NANO LETTERS

Letter

pubs.acs.org/NanoLett

Atomic Structure and Structural Stability of $Sc_{75}Fe_{25}$ Nanoglasses

J. X. Fang,*[,†,‡] U. Vainio,[§] W. Puff,[∥] R. Würschum,[∥] X. L. Wang,[‡] D. Wang,[†] M. Ghafari,[†] F. Jiang,*[,‡] J. Sun,[‡] H. Hahn,[†,⊥] and H. Gleiter*[,†]

[†]Institute for Nanotechnology, Karlsruhe Institute of Technology (KIT), Karlsruhe 76021, Germany

[‡]State Key Laboratory for Mechanical Behavior of Materials and MOE Key Laboratory for Nonequilibrium Synthesis and Modulation of Condensed Matter, Xi'an Jiaotong University, Shann Xi, 710049, People's Republic of China

[§]HASYLAB at DESY, Notkestr. 85, D-22607 Hamburg, Germany

[∥]Institut für Materialphysik, Technische Universität Graz, Petersgasse 16, A-8010 Graz, Austria

[⊥]Joint Research Laboratory Nanomaterials, Technische Universität Darmstadt, Petersenstr. 32, 64287 Darmstadt, Germany

Supporting Information

ABSTRACT: Nanoglasses are solids consisting of nanometer-sized glassy regions connected by interfaces having a reduced density. We studied the structure of $Sc_{75}Fe_{25}$ nanoglasses by electron microscopy, positron annihilation spectroscopy, and small-/wide-angle X-ray scattering. The positron annihilation spectroscopy measurements showed that the as-prepared nanoglasses consisted of 65 vol% glassy and 35 vol% interfacial regions. By applying temperature annealing to the nanoglasses and measuring in situ small-angle X-ray scattering, we observed that the width of the interfacial regions increased exponentially as a function of the annealing temperature. A quantitative fit to the small-angle X-ray scattering data using a Debye−Bueche random phase model gave a correlation length that is related to the sizes of the interfacial regions in the nanoglass. The correlation length was found to increase exponentially from 1.3 to 1.7 nm when the sample temperature was increased from 25 to 230 °C. Using simple approximations, we correlate this to an increase in the width of interfacial regions from 0.8 to 1.2 nm, while the volume fraction of interfacial regions increased from 31 to 44%. Using micro-compression measurements, we investigated the deformation behavior of ribbon glass and the corresponding nanoglass. While the nanoglass exhibited a remarkable plasticity even in the annealed state owing to the glass-glass interfaces, the corresponding ribbon glass was brittle. As this difference seems not limited to $Sc_{75}Fe_{25}$ glasses, the reported result suggest that nanoglasses open the way to glasses with high ductility resulting from the nanometer sized microstructure.

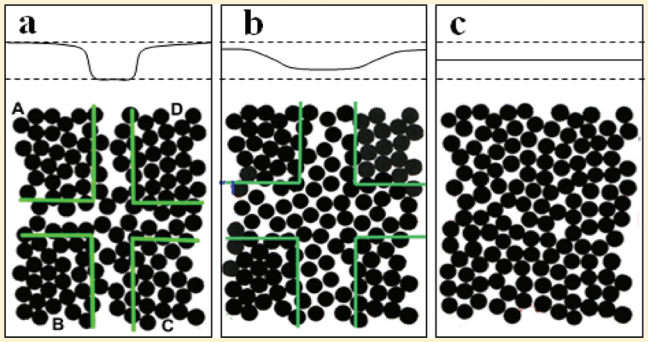

KEYWORDS: *Nanoglass, metallic glass, small-angle X-ray scattering, wide-angle X-ray scattering, positron annihilation spectroscopy, interface delocalization, mechanical property*

Nanoglasses are amorphous solid materials produced by the consolidation of nanometer-sized glassy clusters. The microstructure of nanoglasses has been proposed to consist of nanometer-sized glassy regions and interfaces between them, called glass−glass interfaces. These interfaces are characterized by a reduced density relative to the density in the glassy regions.[1−4] Up to now, a variety of nanoglasses with chemical compositions Au−Si, Au−La, Fe−Si, La−Si, Pd−Si, Ni−Ti, Ni−Zr, and Ti−P have been synthesized by inert gas condensation.[2−4] Structural studies applying transmission electron microscopy (TEM), Mössbauer spectroscopy,[4] and small-angle X-ray scattering[5] agree with the proposed microstructure. Recent molecular dynamic (MD) simulations[1,6] indicate that, when nanoglasses are annealed, the free volume that is initially located in the glass−glass interfaces starts to delocalize so that wider regions with reduced density are formed. No analogous delocalization process occurs in nanocrystalline/polycrystalline materials.[7] Thus, nanoglasses, due to their tunable structure, are expected to show new effects, e.g., concerning mechanical or magnetic properties and tunable diffusivity or electric/thermal conductivity, and to attract a broader community, such as nanomaterials and metallic glasses as well as various property exploitations. Therefore, nanoglasses represent a class of materials where the atomic structure of which may be tuned by controlling the volume fraction of the glass−glass interfaces in the as-consolidated nanoglasses and by modifying the degree of delocalization by varying the annealing time and/or temperature.

However, so far little is known about the atomic structure of the glass−glass interfaces, and no direct experimental evidence for their delocalization during annealing has been presented. In

Received: October 31, 2011
Revised: November 23, 2011
Published: November 28, 2011

this Letter, as a seminal piece of work, we demonstrated the direct experimental evidence of the delocalization process by investigating the atomic structure of as-prepared as well as of annealed $Sc_{75}Fe_{25}$ nanoglasses by means of TEM, in situ small- and wide-angle X-ray scattering (SAXS/WAXS), local chemical analysis, and positron annihilation spectroscopy (PAS). Using mircocompression measurements, we investigated the mechanical deformation behavior of ribbon glass and nanoglass for the as-prepared and annealed states.

$Sc_{75}Fe_{25}$ nanoglass specimens were produced by inert-gas condensation (IGC) in a system described in refs 4 and 5. An ultra-high-vacuum (UHV) system at 10^{-8} to 10^{-9} mbar base pressure was filled with high purity He (99.9999%) at pressures between 2 and 10 mbar. The Sc−Fe alloy was prepared by arc melting pure Sc and Fe using an initial composition of $Sc_{65}Fe_{35}$. This alloy was evaporated from a tungsten boat via the IGC process. The evaporated material condensed in the He atmosphere in the form of nanometer-sized amorphous spheres. The spheres were collected at the surface of a rotating liquid nitrogen-cooled cylinder, subsequently they were stripped off the cylinder and then transferred to an in situ high-pressure consolidation system. Consolidation was performed in two steps: In the first step, the powder was consolidated in the UHV system (at 10^{-8} mbar) at 1.5 GPa pressure for 5 min. The resulting specimens had the shape of a disk with a diameter of 8 mm and thickness between 200 and 400 μm. The disks were sealed in paraffin at 10−8 mbar. In the second step, the disks were further consolidated at various pressures of either 1.5, 3.0, or 4.5 GPa.

The TEM observations were performed with a FEI Titan 80−300 operated at 300 kV. Loose powder samples were prepared by placing a carbon-coated TEM grid onto the coldfinger in the inert gas condensation chamber. The consolidated specimens were mechanically polished and thinned using a dimpler. In-situ heating experiments using simultaneous SAXS/WAXS were carried out at beamline B1 of the DORIS III synchrotron at DESY. The samples were heated in vacuum (10^{-4} mbar) stepwise (10 K/step), with heating rates of 5 K/min between the steps. Once the desired temperature at each step was reached, the temperature was stabilized for some minutes before a SAXS/WAXS measurement was performed. The time required for one measurement was of about 15 min. A 2D Pilatus 300k was used as the SAXS detector. The WAXS measurements were carried out using a 1D Mythen detector. The PAS measurements were performed at ambient temperature for samples that were preannealed at elevated temperatures for 120 min. For the PAS measurements, a conventional lifetime spectrometer was used with a time resolution of 170 ps full width at half-maximum (fwhm). The positron source had a sandwich configuration. This configuration was prepared by depositing about 370 kBq of ^{22}NaCl on a thin Al foil (area density 0.81 mg/cm^2). Each lifetime spectrum was accumulated over a 10 h period, resulting in about 5×10^6 counts in each spectrum. The spectra were analyzed using the PFPOSFIT program, taking into account a source correction for the annihilation of positrons in the Al foil and the ^{22}NaCl source. The structure and chemical composition were characterized using X-ray diffraction (XRD) and energy-dispersive X-ray spectroscopy (EDX) (Figures S1−2, Supporting Information). The thermal stability was investigated by differential scanning calorimetry (DSC) (Figure S3, Supporting Information). Similar DSC studies were performed using melt-spun ribbons with the same chemical composition as a reference. The uniaxial microcompression testing was performed using a Hysitron TI 950 TriboIndenter with a diamond flat punch 10 μm 60° conical tip (the top of the tip is 10 μm in diameter and the cone angle is 60°) under both loading control (100 μNs^{1-}) and displacement control (an initial nominal strain rate of 10^{-4} s^{-1}) modes. Cylindrical micropillars with nominal sizes of 2 μm in diameter and 5 μm in height from both the glassy ribbon and the nanoglass were fabricated using an FEI dual beam focused ion beam (FEI Helios NanoLab) system. A high Ga ion beam current (30 keV and 21 nA) was used for rough cutting, and the beam current was gradually decreased to 28 pA for machining of the final pillar. The sidewall tapering angle is less than 3° because of the sputtering process. The smallest diameter exists at the column top. The smallest areas of cross sections at the top of micropillars were measured for the calculation of stress. The morphology of compressed pillar samples was also observed with the focused ion beam.

Figure 1a shows a TEM micrograph of loose $Sc_{75}Fe_{25}$ glassy spheres (diameter ~7 nm) deposited onto a carbon film. Figure

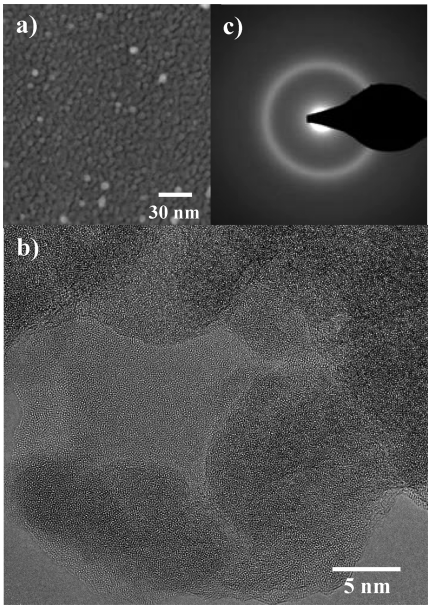

Figure 1. TEM and HRTEM micrographs of a $Sc_{75}Fe_{25}$ nanoglass. (a) Loose powder of the glassy spheres that were used to produce the nanoglass by consolidation. (b) HRTEM image of a nanoglass specimen consolidated with a pressure of 4.5 GPa. (c) Selected area electron diffraction pattern recorded from the region shown in (b).

1b displays the structure of the $Sc_{75}Fe_{25}$ nanoglass produced by consolidating at 4.5 GPa. The thickness contrast (bright/dark regions) indicates a microstructure consisting of nanometer-sized regions. The selected area electron diffraction (SAED) pattern (Figure 1c) evidence its amorphous structure. In fact, the electron diffraction patterns of the nanoglass and of a melt-spun glass were indistinguishable. Elemental mapping (Figure S4, Supporting Information) was used to get information about the local chemical composition of the nanoglass. Composition of about $Sc_{85}Fe_{15}$ was found in the interfacial region and the compositions ranging from $Sc_{70}Fe_{20}N_{10}$ to $Sc_{50}Fe_{30}N_{20}$ inside of the glassy clusters.

PAS was utilized to examine the distribution of the free volume in the as-prepared as well as in the annealed $Sc_{75}Fe_{25}$ nanoglasses consolidated at 4.5 GPa. The following two lifetime

dx.doi.org/10.1021/nl2038216 | Nano Lett. 2012, 12, 458−463

components were found: τ_1 = 169 and τ_2 = 285 ps (Figure 2a). The mean positron lifetime was 209 ps. Long positron lifetimes in the order of 350−500 ps, as indicators of nanovoids, were not observed. According to the theoretically predicted lifetimes of vacancies in Fe and Sc,[8,9] a lifetime of τ_1 = 169 ps characterizes regions of free volumes smaller than the one of a vacancy, and a lifetime of τ_2 = 285 ps indicates the presence of regions in which the free volume is in the order of about two vacancies. Moreover, the component τ_1 = 169 ps is comparable with the positron lifetime in the melt-spun amorphous ribbons with similar chemical composition.[10,11] Therefore, the τ_1 component was interpreted to originate from the interior of the glassy spheres. The second component (τ_2 = 285 ps) was observed exclusively in the as-consolidated nanoglass. Hence, this component is suggested to originate from the glass−glass interfaces, characterized by an enhanced free volume. According to Figure 2b, the volume fraction of the glass−glass interfaces in the as-prepared $Sc_{75}Fe_{25}$ nanoglass is about 35%. When the $Sc_{75}Fe_{25}$ nanoglass was annealed, the intensity of the τ_1 component decreased from initially 65% to 25% (Figure 2b). Simultaneously, the intensity of the τ_2 component increased from 35 to 75% (Figure 2b). When the nanoglass specimens were annealed above 150 °C (Figure 2a), the lifetimes, τ_1 and τ_2, decreased to values similar to those for pure Sc and pure α-Fe (102−112 ps). These lifetimes agree with the concentration fluctuation revealed by elemental mapping in individual glassy spheres (Figure S4, upper figure, Supporting Information) as well as in the nanoglass after ion beam thinning (Figure S4, lower figure, Supporting Information). In fact, the elemental mapping revealed regions in which one has nearly pure Fe or nearly pure Sc. At annealing temperatures above 150 °C, the mean positron lifetime, τ_m, of the nanoglass decreased (Figure 2a), indicating that average free volume within the nanoglass decreases. This observation agrees with the results of annealing experiments of melt-spun metallic glasses in which the quenched-in free volume is found to be reduced due to structural relaxation processes.[11]

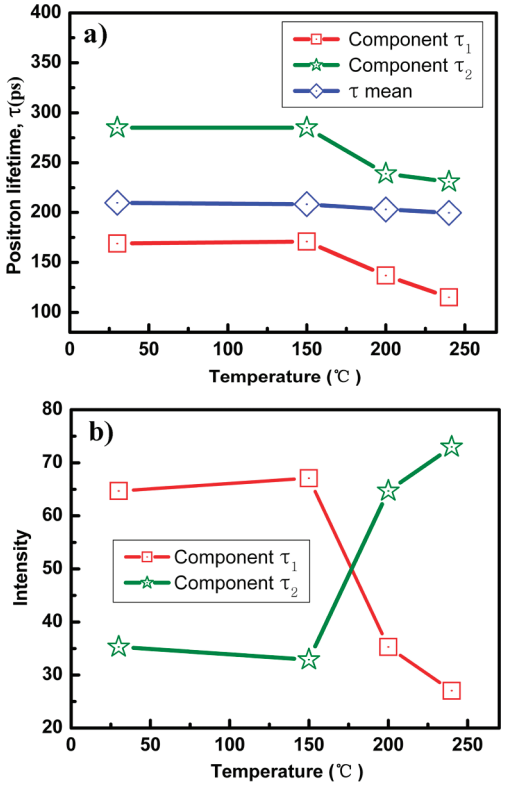

Figure 2. (a) Positron lifetime of components τ_1 (red line), τ_2 (green line) and mean positron lifetime τ_m (blue line) of the nanoglass. (b) Relative intensities I_1, I_2 ($I_1 = 100 - I_2$) of the same components in the as-prepared state of the $Sc_{75}Fe_{25}$ nanoglass and during annealing of the same nanoglass.

In order to study the structural changes occurring in nanoglasses during annealing in more detail, SAXS/WAXS

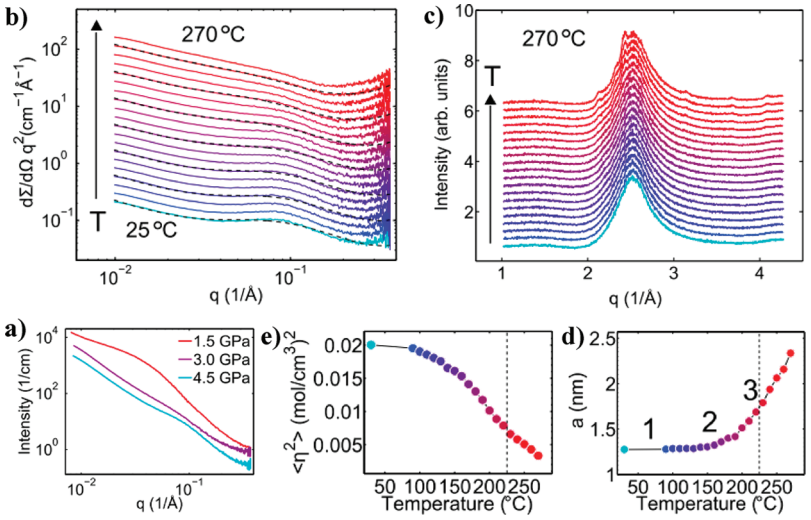

Figure 3. (a) SAXS curves of $Sc_{75}Fe_{25}$ nanoglasses consolidated at different pressures. The SAXS intensity has been multiplied by q^2 to show the hump more clearly. The 3.0 GPa curve has been shifted for clarity. (b) q^2-Weighted SAXS curves of a 4.5 GPa $Sc_{75}Fe_{25}$ nanoglass as a function of annealing temperature (see details in Figure S6, Supporting Information). The curves have been shifted for clarity, except for the lowest curve. (c) Corresponding WAXS curves from the same sample. The curves have been shifted for clarity. (d) and (e) Results of the Debye−Bueche fit to SAXS data. The error bars of this fit are smaller than the sizes of the markers. The vertical dashed lines indicate the temperature at which crystallization was observed to start. The length of the scattering vector q is defined as $4\pi \sin(\theta)/\lambda$, where θ is half of the scattering angle and λ is the wavelength.

dx.doi.org/10.1021/nl2038216 | Nano Lett. 2012, 12, 458−463

measurements were carried out by using $Sc_{75}Fe_{25}$ nanoglasses consolidated under different pressures: The consolidation pressures used were: 1.5 (sample A), 3.0 (sample B), and 4.5 GPa (sample C). The SAXS curves displayed in Figure 3a are composed of two components: a power-law component and a superimposed hump. Power-law components are known to originate from fractal fluctuations of the electron density in the interior of the specimen and/or from surface roughness.[12] The observation of the hump suggests that the structure of the nanoglass may be modeled as a two component system consisting of regions of high density and regions of lower density. In fact, the experimental data were fitted (as suggested by the MD results as well as by the TEM observations, Figure 1) by assuming the nanoglass to consist of spherical regions having all the same density and a log normal size distribution. When a fit of the experimental data with this kind of a model was carried out, we obtained mean sphere diameters of 5.4 nm for sample A and about 3.0 nm for samples B and C. As the diameter of glassy spheres was about 7 nm (TEM observations), the humps in SAXS curves may be interpreted as being related to the sizes of the glassy regions and their interconnecting interfaces.

Figure 3 shows the results of the SAXS/WAXS measurements during the in situ stepwise annealing of a specimen consolidated at 4.5 GPa (see detailed process in Figure S6, Supporting Information). As may be seen from Figure 3b, during annealing, the intensity of the hump decreases when the specimens are annealed at 230 °C or less. At annealing temperatures above 230 °C, the $Sc_{75}Fe_{25}$ nanoglass started to crystallize (Figure 3c). The negative volume expansion in WAXS (Figure S7, Supporting Information) indicates a decrease in total free volume of the nanoglass.

Assuming a random two-phase model of high and low density areas, for samples B and C, the SAXS data obtained during in situ heating were fitted ($\chi^2/(N-f) < 15$) by using a Debye–Bueche model[13] and a power-law background in absolute intensity units:

$$I(q) = r_e^2 N_A^2 a^3 \frac{8\pi^2\langle\eta^2\rangle}{(1+q^2a^2)^2} + Bq^{-\alpha} + C \quad (1)$$

where $I(q)$ is the intensity in absolute intensity units (cm^{-1}), r_e is the classical electron radius, N_A is the Avogadro number, a is a correlation length, $\langle\eta^2\rangle$ denotes mean square fluctuation in electron density [$(mol/cm^3)^2$], B and C are fitted constants, and $-\alpha$ is the power-law exponent.

The correlation length, a, is related to the thickness of the interfacial regions between the glassy regions and depends on the total surface area S between the glassy regions of high density and the glass–glass interfaces of lower density:[13]

$$a = 4\phi_p\phi_i\frac{V}{S} \quad (2)$$

Here φ_p is the volume fraction of the consolidated glassy regions, φ_i is the volume fraction of the glass–glass interfaces, and V is the total volume of the sample. In an as-consolidated sample, the area S is large because the regions of low density are arranged in the form of the relatively narrow glass–glass interfaces. However, during annealing the width of these glass–glass interfaces increases due to delocalization and simultaneously the diameter of the glassy regions shrink, these structural changes increase φ_i and reduce φ_p as well as S. As φ_p and φ_i vary in opposite directions, the reduction of S is the dominant term controlling the variation of the correlation length during annealing. The experimentally observed correlation length, a, increased from about 1.3 to 1.7 nm when the temperature was increased stepwise up to 230 °C (Figure 3d). In a simplified model of core–shell particles, if one assumes the diameter of the glassy regions to be D_{tot} = 7 nm, the curve displayed in Figure 3d may be fitted with the following equation:

$$a = \frac{2}{3}\phi_i(1-\phi_i)^{1/3}D_{tot} \quad (3)$$

where volume fraction of interface, φ_i, is an exponential function. As is discussed in the Supporting Information, eq 3 is based on approximations that will not hold at high-volume fractions of interface. Using this model, an increase in a from 1.3 to 1.7 nm corresponds roughly to an increase of the interfacial width from 0.8 to 1.2 nm and an increase of the volume fraction of the interfaces from 31 to 44%. Furthermore, an analytical form for φ_i as a function of temperature was found

$$\phi_i = A\exp[(T-T_c)/\tau] + B \quad (4)$$

where A = 0.00031, T_c = 308 K, τ = 31 K, and B = 0.31 with goodness of the fit being $\chi^2/(N-f)$ = 3.4.

The mean square fluctuation of the electron density, $\langle\eta^2\rangle$, characterizes the electron density difference between high- and low-density regions,[14] i.e., between the glassy regions and the glass–glass interfaces:

$$\left\langle\eta^2\right\rangle = \phi_i\phi_p(\rho_p-\rho_i)^2 \quad (5)$$

Here ρ_i and ρ_p are the electron densities in the glass–glass interfaces and in the glassy regions, respectively. Variations in $\langle\eta^2\rangle$ (Figure 3e) may be caused either by changes in the relative volume fractions of the glass–glass interfaces and of the glassy regions or by variations of the electron densities within both components or by changes of all of these parameters. According to Figure 3e, a gradual decrease of $\langle\eta^2\rangle$ is observed (Figure 3e) from about 0.02 $(mol/cm^3)^2$ at 100 °C to 0.007 $(mol/cm^3)^2$ at about 230 °C. Using the volume fractions of the glassy regions and the glass–glass interfaces obtained from PAS (Figure 2) combined with eq 5, we find that the difference in electron density between the glass–glass interfaces and inside of the glassy regions is about 17% of the electron density inside glassy regions in the as-consolidated state. A fraction of this electron density difference results from the different chemical compositions of the interfaces and the glassy regions. From the element mapping data, we may estimate that the chemical composition of the interfaces was $Sc_{85}Fe_{15}$ whereas the glassy regions had a composition of $Sc_{70}Fe_{20}N_{10}$. This difference leads to a value of $\langle\eta^2\rangle$ of 0.002 $(mol/cm^3)^2$, which corresponds to a 6% lower electron density in the interfaces compared to the adjacent glassy regions, meaning that only about one-third of the electron density difference can be explained by the difference in elemental composition, and the rest is due to free volume in the interfaces. See Supporting Information for details.

The structural evolution of the nanoglass suggested by the observed variation of a and $\langle\eta^2\rangle$ is summarized schematically in Figure 4. In the as-consolidated structure, the glass–glass interfaces have a small interfacial width and a low volume fraction of the interfaces. When the nanoglass is annealed at temperature below 230 °C, the width of the glass–glass

dx.doi.org/10.1021/nl2038216 | Nano Lett. 2012, 12, 458–463

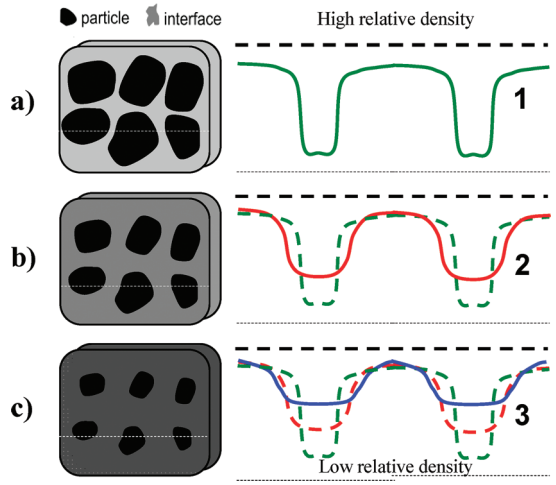

Figure 4. (a) Schematical structural model of the $Sc_{75}Fe_{25}$ nanoglass during annealing according to the results of PAS and SAXS/WAXS. The white dashed lines in (a), (b), and (c) represent the cross section and nos. 1−3 correspond s to the steps 1−3 in Figure 3d. The different dark/bright regions (left side) symbolize the density variation in the glassy regions and in the interfaces between them. Darker regions have a higher density. The curves in the right column of (a), (b), and (c) schematically represent the relative density and its evolution during annealing.

interfaces exponentially increases as a function of temperature. Simultaneously, the relative electron density difference between the glassy and the interfacial regions decreases. The different dark/bright regions (left side) in Figure 4 symbolize the density variation in the glassy regions and in the interfaces between them. Darker regions have a higher density. The curves in the right column of (a), (b), and (c) schematically represent the relative density and its evolution during annealing. In other words, the free volume that is initially localized in the glass−glass interfaces is spread out (i.e., it delocalizes) increasing the widths of these interfaces and reducing their free volume. A similar process is not observed in intercrystal boundaries because solitons are stable in crystal but not in glasses due to the vanishing shear modulus of glasses at infinite times.[15] For example, the width of a dislocation is inversely proportional to the shear modulus, G, and hence the dislocation delocalizes if G vanishes.

If these observations are compared with MD results for CuZr,[6] then the following discrepancies are apparent. The MD results suggest that in metallic glasses delocalization occurs—even at low temperatures—within a few picoseconds. A completely homogeneous composition as predicted by MD was, however, not observed experimentally. One reason for this discrepancy could be the chemically inhomogeneous microstructure of the as-consolidated $Sc_{75}Fe_{25}$ nanoglasses (Figure S4, Supporting Information). To achieve a fully homogenious solid during annealing, two processes are needed: (1) local atomic rearrangements, in order to delocalize the free volume of the glass−glass interfaces, and (2) long-range diffusion processes,[16] in order to remove the fluctuations of the chemical composition.

The large number of glass−glass interfaces in nanoglasses is expected to change the properties of these glasses, for example, the plasticity, compared to their homogeneously glassy counterparts. Recent MD simulations of a nanoglass were carried out using the Mendelev's embedded atom-type potential for $Cu_{64}Zr_{36}$ metallic glasses.[17] Two types of glasses, i.e., bulk metallic glass (BMG) and nanoglasses, with the same geometry were generated. Subsequently, the structures were deformed under uniaxial tension parallel to the z-direction at 50 K with a constant strain rate of 4×10^7 1/s. The local atomic shear strain for a BMG in comparison with as-prepared nanoglass and annealed nanoglass is displayed in Figure 5a.

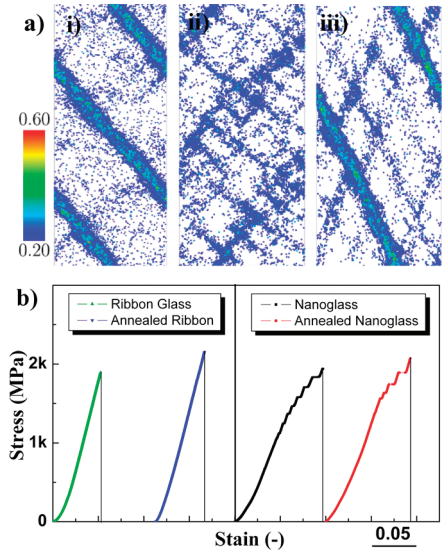

Figure 5. (a) MD simulation of local atomic shear strain for a $Cu_{64}Zr_{36}$ bulk metallic glass (i) in comparison with local atomic shear strain for corresponding as-prepared nanoglass (ii) and annealed nanoglass (iii) under tensile deformation with the same chemical composition.[17] (b) Stress−strain curves of $Sc_{75}Fe_{25}$ ribbon glasses and nanoglasses for as-prepared and annealed states. Annealing was conducted at 200 °C for 2 h.

One can see that the BMG showed an inhomogenous deformation, exhibiting localized deformation in one major shear band (Figure 5a,i). However, the deformation in as-prepared nanoglass is homogeneous owing to the formation of multiple shear bands in the glass−glass interfaces (Figure 5a,ii). Even if the nanoglass was annealed, due to the deviation between the atomic structures of both glasses, a different shear band structure relative to the corresponding bulk glass was still obtained (Figure 5a,iii).[17] The MD results imply that nanoglasses could show an improved mechanical performance compared with their bulk metallic glass counterparts. Although the strain rates used in the MD simulations and in the experiments differ by several orders of magnitude, the results are known to be comparable unless the deformation process does involve thermally activated steps with a high activation enthalpy. Thermal activation is negligible in the deformation processes discussed here.

In this work, using the microcompression testing, we investigated the deformation behavior of the $Sc_{75}Fe_{25}$ BMG, as-prepared $Sc_{75}Fe_{25}$ nanoglass and annealed $Sc_{75}Fe_{25}$ nanoglass, as shown in Figure 5b, respectively. The glassy ribbon exhibits brittle fracture at a strain of around 5% and a stress of about ∼1900 and ∼2200 MPa for the as-prepared and annealed states, respectively. This behavior in is completely different in a corresponding $Sc_{75}Fe_{25}$ nanoglass, as shown in Figure 5b. $Sc_{75}Fe_{25}$ nanoglass in the as-consolidated state yields at a lower stress than the glassy ribbons, i.e., at a stress of about 1250 MPa. After the yield point, the nanoglass shows nonlinear

dx.doi.org/10.1021/nl2038216 | Nano Lett. 2012, 12, 458−463

plastic flow, i.e., a region of strain-hardening, followed by a fracture stress of about 1950 MPa, comparable to the ribbon glass. Annealing is known to result in the embrittlement of BMGs because it reduces their free volume due to structural relaxation processes.[18] However, owing to the existence of abundant glass−glass interfaces which promote a high number of embryonic shear bands, nanoglass retains still a remarkable compressive plasticity with a slightly increased yield (~1580 MPa) as well as facture strength (~2180 MPa), even though the glass is annealed for a relatively long time, e.g., 2 h at 200 °C. This result is in good agreement with the findings of the MD simulation (Figure 5a,iii), where the annealed nanoglass still shows a different microstructure relative to the BMG thus displays notable plasticity. The increase of yield strength may be attributed either to a reduction of the total free volume or its "delocalization" from the initially localized configuration in the glass−glass interfaces.[6] We note that nanoglasses show a relatively low yield stress both in MD simulation and in experimental measurements. This is acceptable since nanoglasses accommodate a great number of low density regions, i.e., glass−glass interfaces. However, unlike that of the MD results as shown in ref 17, experimentally, nanoglasses display comparable fracture strength relative to the ribbon glass. This would be related to the generation and intersection of multiple shear bands at the glass−glass interfaces which contribute to the obvious plasticity and the enhanced fracture strength.

It may be expected that nanoglasses will not only differ in their mechanical properties from the corresponding bulk glasses but also, for example, in their diffusive, magnetic, and electric properties. In fact, recent studies show that $Sc_{10}Fe_{90}$ nanoglasses are ferromagnetic at ambient temperature with saturation magnetizations above that of α-Fe,[19] whereas the melt-spun glass is paramagnetic. In this regard, the possibility to tune atomic structures of nanoglasses will enable us to modify all atomic structure-dependent properties of this glass. It is believed that nanoglasses with various compositions will be synthesized, and diverse novel properties will be exploited in the near future.[20]

■ ASSOCIATED CONTENT

Supporting Information

Information on the SAXS analysis and Figures S1−S8. This material is available free of charge via Internet at http://pubs.acs.org.

■ AUTHOR INFORMATION

Corresponding Author

*E-mail: jxfang@mail.xjtu.edu.cn; jiangfeng@mail.xjtu.edu.cn; herbert.gleiter@kit.edu.

■ ACKNOWLEDGMENTS

This work was supported by the Deutsche Forschungsgemeinschaft (DFG) under contract HA 1344/23-1. We thank J. Ivaisenko and E. Tõldsepp for helping with measurements, B. Sahoo and J. Bednarcik for helpful discussions, Alexander-von-Humboldt Foundation for a fellowship, and the NES Program at KIT for support. J.X. Fang was supported by National Natural Science Foundation of China (No. 51171139), Doctoral Fund for New Teachers (No.20110201120039), Tengfei Talent Project of Xi'an Jiaotong University, the New Century Excellent Talents in University (NCET) and the Fundamental Research Funds for the Central Universities (No. 08142008). F. Jiang was supported by the National Natural Science Foundation of China under Grant Nos.50871079. J. Sun also wish to express his special thanks for the support from the National Basic Research Program of China (Grant No. 2010CB631003) as well as 111 Project of China (B06025). We also thank the support from the XJTU Center for Advancing Materials Performance from the Nanoscale.

■ REFERENCES

(1) Gleiter, H. *Acta Mater.* **2008**, *56*, 5875.
(2) Gleiter, H. *MRS Bull.* **2009**, *34*, 456.
(3) Würschum, R.; Rollinger, M.; Kisker, H.; Raichle, A.; Damson, B.; Schaefer, H. E. *Nanostruct. Mater.* **1995**, *6*, 377.
(4) Jing, J.; Kramer, A.; Birringer, R.; Gleiter, H.; Gonser, U. *J. Non-Cryst. Solids* **1989**, *113*, 167.
(5) Weissmüller, J.; Birringer, R.; Gleiter, H. *Key Eng. Mater.* **1993**, *77*, 161.
(6) Sopu, D.; Albe, K.; Ritter, Y.; Gleiter, H. *Appl. Phys. Lett.* **2009**, *94*, 191911.
(7) Löffler, J; Weissmüller, J. *Phys. Rev. B* **1995**, *52*, 7076.
(8) Würschum, R.; Badura-Gergen, K.; Kümmerle, E. A.; Grupp, C.; Schaefer, H.-E. *Phys. Rev. B* **1996**, *54*, 849.
(9) Campillo Robles, J. M.; Ogando, E.; Plazaola, F. *J. Phys.: Condens. Matter* **2007**, *19*, 176222.
(10) Würschum, R.; Greiner, W.; Valiev, R. Z.; Rapp, M.; Sigle, W.; Schneeweiss, O.; Schaefer, H.-E. *Scr. Metall. Mater.* **1991**, *25*, 2451.
(11) Nagel, C.; Ratzke, K.; Schmidtke, E.; Wolff, J.; Geyer, U.; Faupel, F. *Phys. Rev. B* **1998**, *57*, 10224.
(12) Lamparter, P.; Steeb, S. *J. Non-Cryst. Solids* **1988**, *106*, 137.
(13) Debye, P.; Anderson, H. R. Jr.; Brumberger, H. *J. Appl. Phys.* **1957**, *28*, 679.
(14) Jánosi, A. *Monatsh. Chem.* **1983**, *114*, 377.
(15) Ch. Kittel. *Introduction to Solid State Physics*; John Wiley & Sons, Inc.: Hoboken, NJ, 1993; p 519.
(16) Faupel, F.; Frank, W.; Macht, M. P.; Mehrer, H.; Naundorf, V.; Ratzke, K.; Schober, H. R.; Sharma, S. K.; Teichler, H. *Rev. Mod. Phys.* **2003**, *75*, 237.
(17) Sopu, D.; Ritter, Y.; Gleiter, H.; Albe, K. *Phys. Rev. B.* **2011**, *83*, 100202 (R).
(18) Launey, M. E.; Busch, R.; Kruzic, J. J. *Acta. Mater.* **2008**, *56*, 500.
(19) Fang, J. X.; Hahn, H.; Gleiter, H. to be published.
(20) Chen, N.; Frank, R.; Asao, N.; Louzguine-Luzgin, D. V.; Sharma, P.; Wang, J. Q.; Xie, G. Q.; Ishikawa, Y.; Hatakeyama, N.; Lin, Y. C.; Esashi, M.; Yamamoto, Y.; Inoue, A. *Acta Mater.* **2011**, *59*, 6433.